**ADVANCED
SCIENCE NEWS**
www.advancedsciencenews.com

NANO MICRO
small

Wearable Electronics

Soft Elastomers with Ionic Liquid-Filled Cavities as Strain Isolating Substrates for Wearable Electronics

Yinji Ma, Matt Pharr, Liang Wang, Jeonghyun Kim, Yuhao Liu, Yeguang Xue, Rui Ning, Xiufeng Wang, Ha Uk Chung, Xue Feng, John A. Rogers, and Yonggang Huang**

Managing the mechanical mismatch between hard semiconductor components and soft biological tissues represents a key challenge in the development of advanced forms of wearable electronic devices. An ultralow modulus material or a liquid that surrounds the electronics and resides in a thin elastomeric shell provides a strain-isolation effect that enhances not only the wearability but also the range of stretchability in suitably designed devices. The results presented here build on these concepts by (1) replacing traditional liquids explored in the past, which have some nonnegligible vapor pressure and finite permeability through the encapsulating elastomers, with ionic liquids to eliminate any possibility for leakage or evaporation, and (2) positioning the liquid between the electronics and the skin, within an enclosed, elastomeric microfluidic space, but not in direct contact with the active elements of the system, to avoid any negative consequences on electronic performance. Combined experimental and theoretical results establish the strain-isolating effects of this system, and the considerations that dictate mechanical collapse of the fluid-filled cavity. Examples in skin-mounted wearable include wireless sensors for measuring temperature and wired systems for recording mechano-acoustic responses.

Dr. Y. Ma, L. Wang, Y. Xue, Prof. X. Wang, Prof. Y. Huang
Department of Civil and Environmental Engineering
Mechanical Engineering, and
Materials Science and Engineering
Northwestern University
Evanston, IL 60208, USA
E-mail: y-huang@northwestern.edu

Dr. Y. Ma, Prof. X. Feng
Department of Engineering Mechanics
Center for Mechanics and Materials
Tsinghua University
Beijing 100084, China

Prof. M. Pharr
Department of Mechanical Engineering
Texas A&M University
College Station, TX 77843, USA

L. Wang
Institute of Chemical Machinery and Process Equipment
Department of Chemical and Biological Engineering
Zhejiang University
Hangzhou 310027, China

Dr. J. Kim, Dr. Y. Liu, R. Ning, H. U. Chung
Department of Materials Science and Engineering
Frederick Seitz Materials Research Laboratory
University of Illinois at Urbana-Champaign
Urbana, IL 61801, USA

Prof. X. Wang
School of Materials Science and Engineering
Xiangtan University
Hunan 411105, China

Prof. J. A. Rogers
Department of Materials Science and Engineering, Chemistry
Mechanical Science and Engineering
Electrical and Computer Engineering
Beckman Institute for Advanced Science and Technology, and
Frederick Seitz Materials
Research Laboratory
University of Illinois at Urbana-Champaign
Urbana, IL 61801, USA
E-mail: jrogers@illinois.edu

1. Introduction

Wearable electronic devices[1–7] are of rapidly increasing interest due to their ability to provide continuous information of relevance to fitness and activity, with ultimate capabilities that have the potential to extend to clinically relevant measurements of health status. For these latter purposes, most modes of measurement demand intimate electrical, thermal, and mechanical interfaces to the body, typically through skin-mounted configurations.[8–11] For comfortable, noninvasive operation in such scenarios, the materials and mechanics designs must yield devices with physical attributes that place minimal constraints on the natural motions and processes of the underlying biological tissues.[12,13] To address this challenge, research focuses on the development of material and device components for soft, stretchable forms of electronics, in approaches that rely either on organic materials, inorganic nanomaterials or composites of these two,[14–22] or on overall structures of materials that are deterministically engineered to afford elastic mechanical responses with low effective moduli.[23–33] Certain advanced strategies of this latter type exploit ultrasoft materials or liquids to surround hard electronic components and interconnects, as a way to strain-isolate them from their interfaces to the body.[34] Although liquids are preferred for this purpose, previously explored combinations of materials had the capacity to leak slowly and to dry out over time. Additionally, direct contact of the liquids with the active electronics created risks in degrading the operational properties.

This paper introduces simple strategies that retain the exceptionally effective strain-isolation capabilities afforded by liquids but without these two drawbacks. Here, an ionic liquid fills a microfluidic space, or cavity, defined in a low modulus elastomeric substrate, as in **Figure 1**a. The contained liquid film mechanically isolates the underlying skin from the electronics above, without any direct contact to either. The use of ionic liquids with negligible vapor pressure and permeability through the classes of elastomers exploited in stretchable electronics (e.g., various formulations of silicones and others) yields robust, long-lived behavior without leakage or evaporation. As examined in combined theoretical and experimental work, this liquid layer also helps to prevent mechanical collapse of the cavity enclosure. The results identify all of the key materials and mechanics variables associated with these systems. Simple examples of skin-mounted wired and wireless sensor systems illustrate the use of these ideas in wearable electronics.

2. Results and Discussions

Figure 1a presents a schematic cross-sectional illustration of the geometry of the system, in which a thin layer of ionic liquid lies between the skin and a stiff electronic device
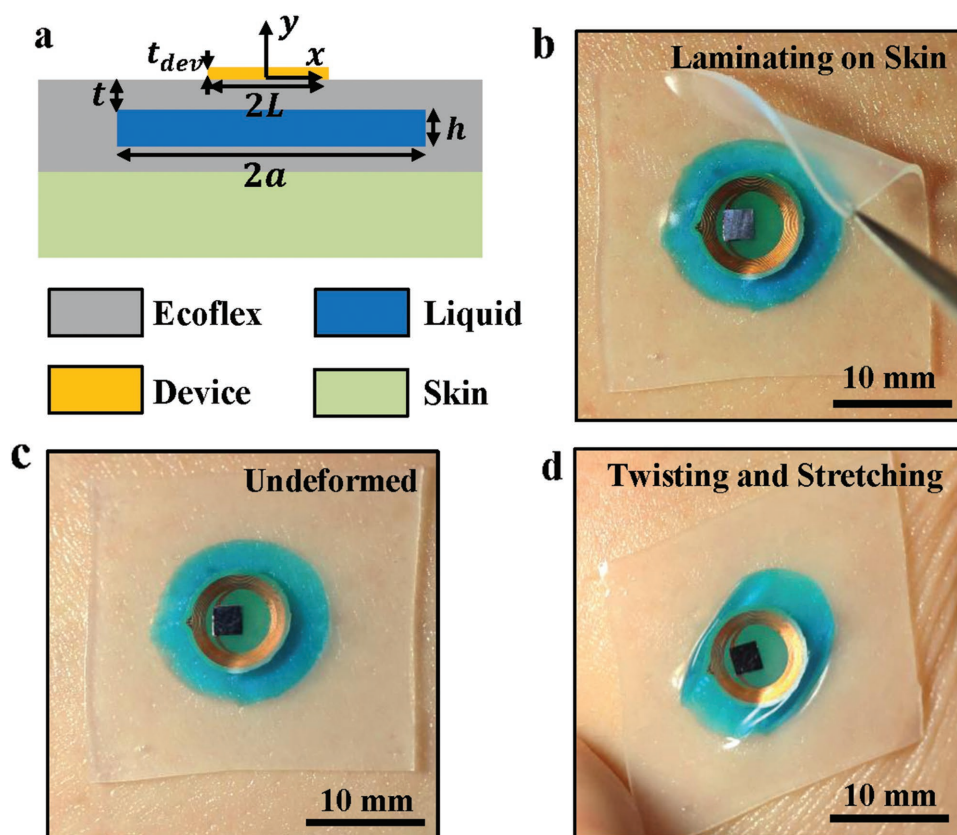

Figure 1. Schematic illustration and pictures of a wearable, skin-mounted device that includes a liquid-filled substrate as a strain isolating support for a wireless electronic sensor that uses near field communication (NFC) technology. a) Cross-sectional schematic illustration of the system on skin. b–d) Integration on a human forearm (b) while laminating on the skin, (c) in the initial undeformed state, and (d) under twisting and stretching deformation. The use of ionic liquid (dyed blue) ensures stable operation, without leakage or evaporation.

(with length $2L$ and thickness t_{dev}), housed in a soft elastomeric enclosure that simultaneously serves as an encapsulation layer for the entire system. The cavity (with length $2a$ and height h) in the elastomer (Ecoflex 00–30, Smooth-On, Macungie, Pennsylvania, elastic modulus $E_{Eco} = 60$ kPa and Poisson's ratio $\upsilon_{Eco} = 0.5$, top Ecoflex thickness t) contains ionic liquid (1-ethyl-3-methylimidazolium ethyl sulfate [EMIM][EtSO$_4$], dyed blue here for clarity, Sigma-Aldrich, St. Louis, Missouri), introduced by syringe injection. Ionic liquids are attractive due to their negligible vapor pressures and permeabilities through many elastomers,[35,36] Indeed, tests reveal excellent stability of this particular ionic liquid in our elastomer, even at elevated temperatures (up to 180 °C, Figure S1, Supporting Information) and for extended periods of time (11 months and ongoing, Figure S2, Supporting Information). By comparison, water readily diffuses through the elastomer and evaporates into the ambient environment (Figure S1, Supporting Information). For thin cavities and substrates ($h \approx 100$ μm and $t \approx 100$ μm) water completely evaporates in a few hours at room temperature and a few minutes at elevated temperatures. Additionally, the specific ionic liquid ([EMIM][EtSO$_4$]) selected for experiments reported here has numerous desirable characteristics: (1) it is a nonirritant to skin and eyes, nonharmful in terms of acute oral toxicity, nonsensitizing, and nonmutagenic,[35] (2) it has a low melting point (< −20 °C), high thermal stability, and high chemical stability, (3) it is optically transparent (dyed blue in this manuscript for emphasis), (4) it has relatively low electrical conductivity, such that it can be incorporated into near-field communication (NFC) wireless systems with negligible signal loss, and (5) it is available commercially at low cost, i.e., $370/kg or ≈$0.016/sample for the geometry shown in Figure 1b–d.[35,36] Figure 1b–d shows optical images of this type of system configured for strain-isolation (Ecoflex substrate, $t = 300$ μm, $2a = 15$ mm, $h = 200$ μm) and integrated with a wireless device that exploits NFC technology ($2L = 8$ mm, $t_{dev} \approx 100$ μm) during the process of soft lamination onto the skin of the forearm, in an initial undeformed state, and under twisting and stretching deformation. The device remains adhered to the skin and it is imperceptible, from the standpoint of skin sensation, under various modes of deformation (Figure 1b–d, and Figures S3 and S4, Supporting Information).

To demonstrate the key mechanical effects of this design strategy, we compare a strain-isolating, liquid-filled structure (Ecoflex, $2a = 15$ mm, $t = 500$ μm, $h = 200$ μm, and 100 μm bottom Ecoflex encapsulation) to a standard structure (no cavity, Ecoflex with the same total initial thickness (0.8 mm) as that of the liquid-filled counterpart). The structures incorporate a rigid test device (packaged NFC chip, Cu coil, and polyimide substrate with $2L = 10$ mm and $t_{dev} \approx 1$ mm), and they laminate onto the surface of a phantom skin sample (Ecoflex, 2 mm thickness, patterned with a square array of fiducial markers with 1.875 mm spacing to highlight the deformation). Details of the fabrication process can be found in Figure S5 (Supporting Information) and in the Experimental Section. **Figure 2** presents optical images and computed stress distributions on the phantom skin for the liquid-filled (left column) and standard (right column) structures, under

50% stretching. The deformations of the square arrays of fiducial markers are nearly identical in the experiments (Figure 2a,b) and finite element analysis (FEA, ABAQUS commercial software, ABAQUS Inc.[37]) simulations (Figure 2c–f) for both liquid-filled and standard substrates. The liquid-filled case demonstrates uniform separation of the fiducials whereas the standard case demonstrates a nonuniform field of deformation, thereby indicating that the liquid-filled system places less constraint on the phantom skin than the standard case. Additionally, from the computations, the shear and normal stresses (Figure 2c,e) on the phantom skin for the liquid-filled case are less than 2 kPa (threshold for sensation in extreme skin sensitivity[38,39]), i.e., they are below the threshold of sensation for extremely sensitive skin. By comparison, Figure 2d,f shows the shear and normal stresses on the phantom skin for the standard case, which exceed this threshold. The corresponding strain distributions on the devices for both cases are shown in Figure 2g,h, which indicate that the liquid-filled design also eliminates strain on the device under stretching of the skin. This reduction in strain on the device additionally aids in preventing delamination between the device and the substrate.

Results for bending appear in Figure S6 (Supporting Information). Figure S6a (Supporting Information) shows the moment–curvature curves obtained by bending the substrate (with a device and without phantom skin) directly for the liquid-filled and standard cases, respectively. The bending stiffness of the liquid-filled case reduces to ≈½ of that of standard case. Figure S6b–e (Supporting Information) shows the shear and normal stresses on the phantom skin for bending (0.05 mm^{-1} applied curvature) when bent through the phantom skin. The interfacial stresses for the liquid-filled case (Figure S6b,d, Supporting Information) are under 2 kPa and are much smaller than those for the standard case (Figure S6c,e, Supporting Information). Furthermore, the results in Figures S7 and S8 (Supporting Information) demonstrate that liquid-filled structures for strain-isolation are superior to previously reported core/shell structures[12] (for the same total initial thickness) under both stretching (30%) and bending (0.05 mm^{-1} applied curvature). Overall, this new design approach substantially reduces both the interfacial stresses between the substrate and the skin and the mechanical constraints caused by the device while simultaneously shielding the device from strains associated with natural body motions.

An important consideration is that layers of elastomer above and below the cavity can potentially come into contact and adhere to one another (**Figure 3**a,b),[40] through a process that we refer to as roof collapse. Roof collapse substantially diminishes the strain-isolation effects; thus, the systems should be designed to avoid such collapse. We first examine collapse of cavities (length $2a$ and height h) without overlying devices to establish the governing mechanics and compare behaviors for cases with air (Figure 3a) and liquid (Figure 3b). The deformation energy in a semi-infinite substrate of elastomer below the cavity is negligible compared to that in the layer (thickness t) above the cavity (see Note 1 and Figure S9 of the Supporting Information for details). Therefore, roof collapse of the cavity occurs mainly due to
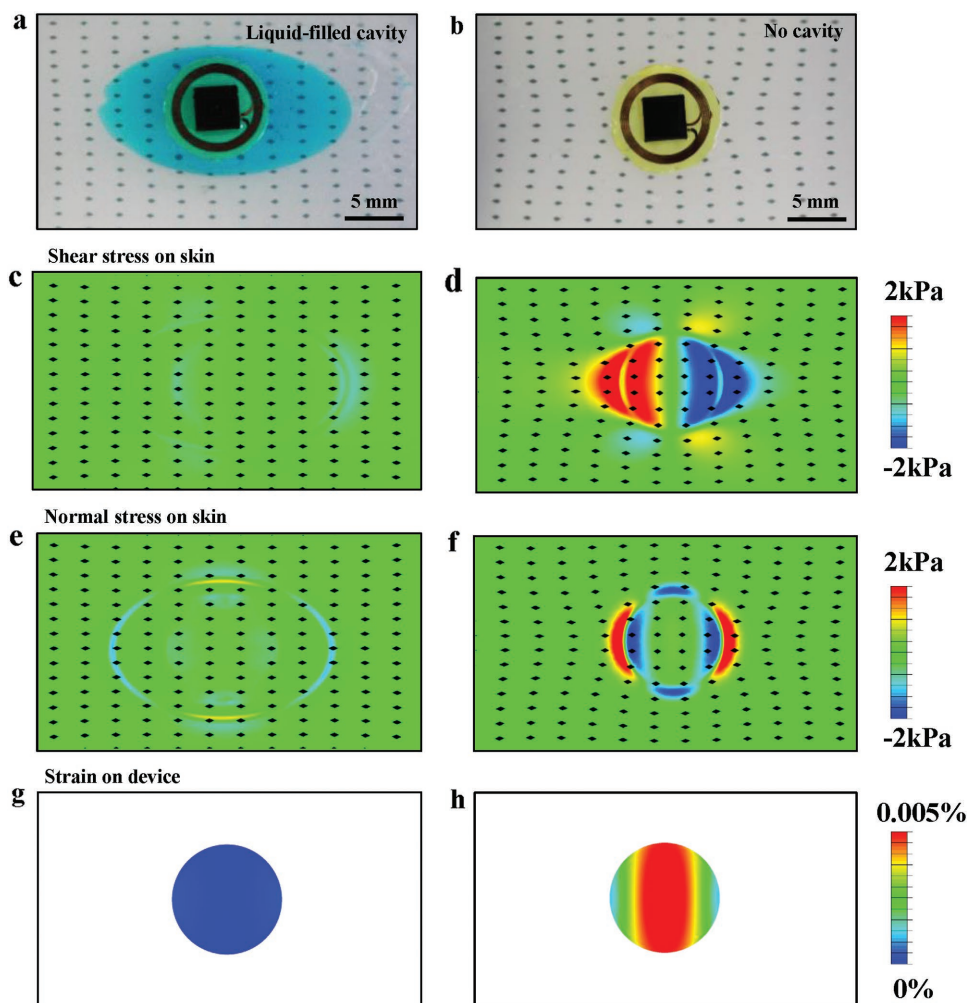
Figure 2. Comparison of wireless, NFC devices during stretch with and without a strain-isolating substrate. a,b) Top view of an NFC device on phantom skin stretched to 50% (a) with and (b) without a liquid-filled cavity. The fiducial markers show the deformation at the interface between the phantom skin and the device. c–f) Corresponding computational results for the interface–shear stress (c) with and (d) without a liquid-filled cavity, normal stress (e) with and (f) without a liquid-filled cavity. g,h) Computed strain distribution on the NFC device (g) with and (h) without a liquid-filled cavity.

deformation of this top layer. With the uncollapsed configuration (Figure S10, Supporting Information) defined as the ground state (i.e., zero energy), the total potential energy (per unit width in the out-of-plane direction) due to roof collapse is[40]

$$U_{\text{total}} = U_{\text{deformation}} - 2b\gamma \tag{1}$$

where $U_{\text{deformation}}$ is the deformation energy of the top layer and γ is the work of adhesion between the top and bottom surfaces of the cavity. The collapsed region ($|x| \leq b$ in Figure 3a,b) has an adhesion energy $-2b\gamma$ but no deformation energy. The uncollapsed regions ($b < |x| < a$ in Figure 3a,b) are modeled as beams, with one end clamped and the other end subjected to zero rotation and deflection $-h$. For the air-filled cavity, the uncollapsed regions are traction free. For the liquid-filled cavity, the extruded liquid from the collapsed region flows into the uncollapsed regions, which creates some liquid pressure across the uncollapsed regions, consistent with conservation of the volume of the liquid. The normalized

total potential energies, $a^3 U_{\text{total}}/(Dh^2)$, are obtained as (see Note 2 of the Supporting Information for details)

$$\frac{a^3 U_{\text{total}}}{Dh^2} = \frac{12}{\left(1 - \left(\frac{b}{a}\right)\right)^3} - 2\overline{\gamma}\frac{b}{a} \tag{2a}$$

$$\frac{a^3 U_{\text{total}}}{Dh^2} = \frac{48\left(4 + 7\left(\frac{b}{a}\right) + 4\left(\frac{b}{a}\right)^2\right)}{\left(1 - \left(\frac{b}{a}\right)\right)^5} - 2\overline{\gamma}\frac{b}{a} \tag{2b}$$

for air-filled and liquid-filled cavities, respectively, where $D = E_{\text{Eco}}t^3/(12(1 - v_{\text{Eco}}^2))$ is the plane-strain bending stiffness of the top layer, and $\overline{\gamma} = a^4\gamma/(Dh^2)$ is the normalized work of adhesion. Figure 3c,d shows the normalized total potential energy $a^3 U_{\text{total}}/(Dh^2)$ versus normalized collapse length b/a with several normalized values for the work of adhesion for air-filled and liquid-filled cavities, respectively.
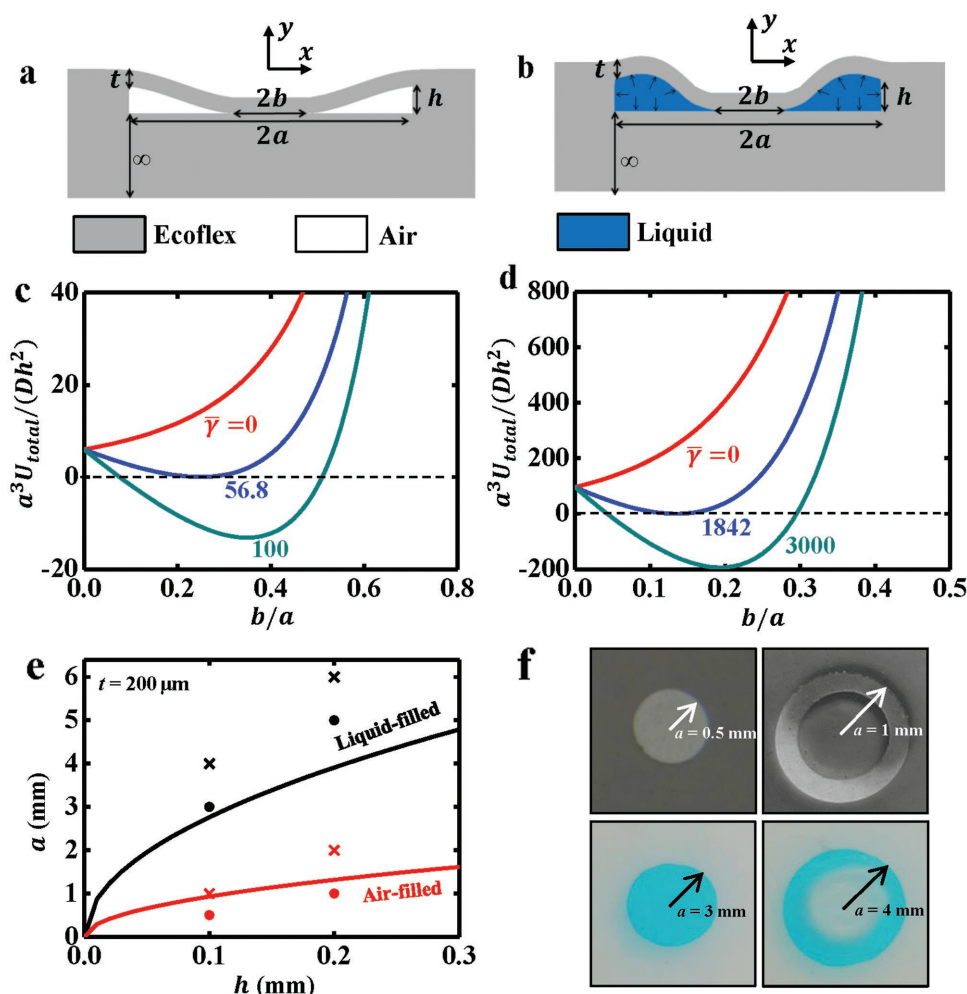
Figure 3. Comparison of the collapse of air-filled and liquid-filled cavities. a,b) Schematic illustrations of collapse of cavities filled with (a) air and (b) liquid. c,d) Normalized total potential energy ($a^3 U_{total}/(Dh^2)$) versus normalized collapse length (b/a) with several normalized values of the work of adhesion ($\overline{\gamma}$) for (c) air-filled and (d) liquid-filled cavities. e) Critical half-length a of the cavity as a function of the cavity height h obtained by the analytic model (solid lines) and the corresponding experimental measurements—the cross symbols ($\times$) represent samples that collapsed while the solid circles ($\bullet$) represent samples that did not collapse. f) Photographs showing transition from no collapse to collapse for cavities filled with air (top) and ionic liquid (bottom).

The normalized total potential energy at $b/a = 0$ exceeds that of the ground state (i.e., the uncollapsed state), thereby suggesting that roof collapse will not occur spontaneously—it instead requires an external stimulus (e.g., an external pressure). The term "roof collapse" mentioned in the following discussion means that the cavity will not return to its uncollapsed state once we remove a perturbing external pressure. For the air-filled cavity (Figure 3c), the minimal total potential energy is positive when the normalized work of adhesion is less than a critical value $\overline{\gamma}_c = 56.8$ such that there is no stable roof collapse for $\overline{\gamma} < \overline{\gamma}_c$ (weak adhesion). For $\overline{\gamma} > \overline{\gamma}_c = 56.8$ (strong adhesion), the collapsed state is stable because the minimal total potential energy is negative. For the liquid-filled cavity (Figure 3d), this critical normalized work of adhesion becomes $\overline{\gamma}_c = 1842$, which is much larger than 56.8 for the air-filled cavity, i.e., the liquid-filled cavity is much less susceptible to collapse.

The adhesion energy of Ecoflex is $\gamma_{Ecoflex} = 20$ mJ m^{-2}.[41] The adhesion energy for the Ecoflex–liquid interface can be estimated as[42]

$$\gamma_{Ecoflex-Liquid} = \gamma_{Ecoflex} - \gamma_{Liquid} \cos \alpha \qquad (3)$$

where γ_{Liquid} is the surface tension of liquid ($\gamma_{Liquid} = 47.8$ mJ m^{-2} for [EMIM][EtSO$_4$][42]) and the contact angle $\alpha = 76°$ is measured by a goniometer as shown in Figure S11 (Supporting Information). The work of adhesion values are $\gamma = 2\gamma_{Ecoflex} = 40$ mJ m^{-2} and $\gamma = 2\gamma_{Ecoflex-Liquid} = 16.8$ mJ m^{-2} (two surfaces disappear during roof collapse of a cavity) for air-filled and liquid-filled cavities, respectively, which, together with the critical normalized values for the work of adhesion ($\overline{\gamma}_c = 56.8$ and 1842 for air-filled and liquid-filled cavities, respectively), give the critical half-length a of the cavity as a function of the cavity height h. These results appear as solid lines in Figure 3e for air-filled and liquid-filled cavities with a fixed 200 µm thick top elastomer layer (t). Roof collapse occurs if the half-length of the cavity is above this critical value. Figure 3f shows the experimental evaluation of cavity roof collapse with a fixed cavity height ($h = 100$ µm) and top layer thickness ($t = 200$ µm). For air-filled cavities, a cavity with a 0.5 mm radius does not

collapse, as evidenced by the uniform contrast over the cavity region in the top left image of Figure 3f. By comparison, a cavity with a 1 mm radius does collapse, as evidenced by the annular area of varying contrast in the top right image of Figure 3f. For liquid-filled cavities, a cavity with a 3 mm radius does not collapse, as evidenced by the blue-dyed ionic liquid filling the entire cavity in the bottom left image of Figure 3f. By comparison, a cavity with a 4 mm radius does collapse, as evidenced by the absence of liquid in the center region in the bottom right image of Figure 3f. Figure S12 (Supporting Information) shows the corresponding roof collapse experiments for a different fixed cavity height ($h = 200$ μm) and the same top elastomer layer thickness ($t = 200$ μm) for air-filled and liquid-filled cavities. In all of these experiments, if we apply an external pressure to force the cavities to collapse, the cavities with small diameters (solid circles in Figure 3e) immediately return to their initial uncollapsed state upon removal of the external pressure. In other words, the cavities with small diameters remain stable even after external perturbations. These experimental results agree reasonably well with the theory as shown in Figure 3e. The slight discrepancies between the theoretical and experimental results for the liquid-filled cavities may result from: (1) the reference values used for $\gamma_{Ecoflex}$ and γ_{Liquid} in Equation (3) may differ from the actual values of the materials used in the experiments or (2) the 2D plane-strain approximation used in the analytical model is simplified, compared to the circular cavities used in the experiments. Overall, these calculations and experiments demonstrate that filling the cavities with liquid significantly aids in preventing roof collapse. As a practical consequence, strain-isolation can be provided with thinner substrates if the substrates are filled with liquid, as opposed to air.

We now examine structures with overlying devices for use in wearable electronics. Figure S13a,b (Supporting Information) shows the analytic model of roof collapse with a device for a liquid-filled cavity without any stretch. The bottom layer, which encapsulates the liquid, can be as thin as practically possible, and is attached to skin (with relatively large thickness, and elastic modulus larger than that of the elastomer). The top layer and device are modeled as beams with two different cross sections: Section 2 has the elastomer only, and its bending stiffness is $D = E_{Eco}t^3/(12(1-\upsilon_{Eco}^2))$; Section 1 has both the elastomer and a device, and its bending stiffness is ηD, where the η is the bending stiffness ratio given by

$$\eta = \frac{\left(\bar{E}_{dev}t_{dev}^2 - \bar{E}_{Eco}t^2\right)^2 + 4\bar{E}_{dev}t_{dev}\bar{E}_{Eco}t(t_{dev}+t)^2}{\bar{E}_{Eco}t^3\left(\bar{E}_{dev}t_{dev}+\bar{E}_{Eco}t\right)} \quad (4)$$

where $\bar{E}_{Eco} = E_{Eco}/(1-\upsilon_{Eco}^2)$ and $\bar{E}_{dev} = E_{dev}/(1-\upsilon_{dev}^2)$. The collapse length $2b$ (Figure S13b, Supporting Information) is determined by minimizing the total potential energy in Equation (1), though the deformation energy $U_{deformation}$ also depends on the device properties (via Equation (4)) and length $2L$. As shown in Figure S13c (Supporting Information), the critical normalized work of adhesion, above which the collapsed state is stable, now depends on the bending stiffness ratio and normalized length (see Note 3 of the Supporting Information for details)

$$\bar{\gamma}_c = f\left(\eta, \frac{L}{a}\right) \quad (5)$$

For wearable electronics it is desirable for the substrate to be as thin as possible. For representative parameters $2a = 15$ mm, $2L = 10$ mm, and $t_{dev} = 100$ μm, and elastic properties $E_{dev} = 130$ GPa and $\upsilon_{dev} = 0.27$ for silicon,[23] $E_{Eco} = 60$ kPa and $\upsilon_{Eco} = 0.5$, Figure S13d,e (Supporting Information) shows the minimum initial cavity thickness (h_{min}) and total initial thickness of the top layer and cavity ($h_{min} + t$), above which roof collapse does not occur, versus the initial top layer thicknesses (t) without any stretch obtained from Equation (5). Figure S13e (Supporting Information) gives an optimal top layer thickness $t = 0.19$ mm, for which the minimal total initial thickness of the top layer and cavity is $h_{min} + t = 0.32$ mm.

Figure 4a,b shows the analytic model of roof collapse for a strain-isolated system with a device during stretching. The tensile stiffness of Section 1 is much larger than that of Section 2 due to presence of the stiff device, such that stretching is mainly accommodated by Section 2, and the thickness of the layer of elastomer below the device is almost unchanged. The length and thickness in Figure 4a are related to the applied stretch ε by (see Note 4 of the Supporting Information for details)

$$a' = (1+\varepsilon)a, \quad h' = \frac{1}{1+\varepsilon}h, \quad t' = \frac{a-L}{(1+\varepsilon)a-L}t \quad (6)$$

The critical normalized work of adhesion can be obtained from Equation (5) by substituting a, h, and t with a', h', and t' after stretch, respectively, to yield

$$\bar{\gamma}_c = \frac{f\left(\eta', \frac{L}{(1+\varepsilon)a}\right)}{(1+\varepsilon)^6\left(1+\frac{\varepsilon a}{a-L}\right)^3} \quad (7)$$

where $\bar{\gamma}_c$ is the critical value of $\bar{\gamma} = a^4\gamma/(Dh^2)$ (consistent with that in Figure 3 and Figure S13, Supporting Information), f is given in Equation (5) and also Figure S13c (Supporting Information), and the bending stiffness ratio after the stretch is obtained from Equation (4) by replacing t with t', namely,

$$\eta' = \frac{\left(\bar{E}_{dev}t_{dev}^2 - \bar{E}_{Eco}t'^2\right)^2 + 4\bar{E}_{dev}t_{dev}\bar{E}_{Eco}t'(t_{dev}+t')^2}{\bar{E}_{Eco}t'^3\left(\bar{E}_{dev}t_{dev}+\bar{E}_{Eco}t'\right)} \quad (8)$$

For $t_{dev} = 100$ μm, $t = 500$ μm, which is close to the optimized thickness for 20% stretch, as is illustrated in Figure 4d, and for the same elastic properties as in Figure S13d,e (Supporting Information), Figure 4c shows the critical normalized work of adhesion ($\bar{\gamma}_c$) versus the normalized length of the device (L/a) under 0%, 20%, and 50% stretch. Figure S14 (Supporting Information) shows $\bar{\gamma}_c$ versus the normalized thickness of the device (t_{dev}/t) for $L/a = 2/3$. The critical normalized work of adhesion ($\bar{\gamma}_c$) decreases rapidly as the stretch increases, which increases the susceptibility of the cavity to collapse. Figure 4c and
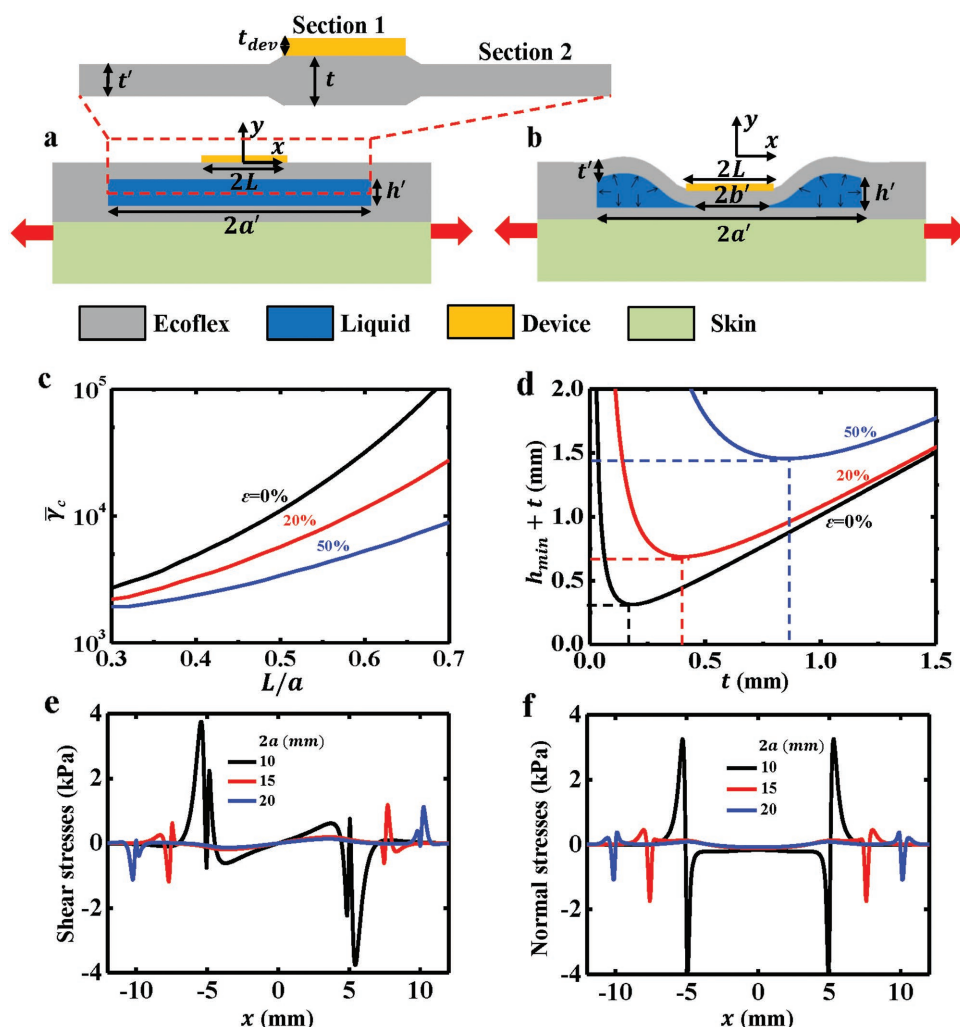
Figure 4. Analysis and optimization of the dimensions of the cavities. a,b) Schematic illustrations of (a) a liquid-filled cavity with a device mounted on the skin and (b) its collapsed state under a stretching deformation. c) Critical normalized work of adhesion ($\overline{\gamma}_c$) versus normalized initial length (L/a) for fixed elastic properties and initial thickness under 0%, 20%, and 50% stretching. d) Minimum total initial thickness ($h_{min} + t$) versus the thickness of the top layer of elastomer (Ecoflex, t). e,f) Interfacial stresses between human skin and the device under 30% stretching for the case of a 10 mm long device with several cavity lengths–(e) shear stress and (f) normal stress as a function of position.

Figure S14 (Supporting Information) suggest that a longer and thicker device helps to avoid roof collapse. Figure 4d shows the minimum total initial thickness of the top layer and cavity ($h_{min} + t$) versus (t) under 0%, 20%, and 50% stretching. For each applied stretch, there exists an optimal top layer thickness t to minimize the total initial thickness $h_{min} + t$, such as $t = 0.43$ mm for 20% stretch. The total initial thickness increases rapidly from 0.32 mm without stretch to 1.45 mm for 50% stretch.

In addition to avoiding roof collapse, it is important to optimize a, h, and t to minimize the stresses on the skin. Figure 4e,f shows the shear and normal stress distributions on the skin (elastic modulus 130 kPa[43]) obtained by FEA for the representative values $h = 200$ μm, $t = 500$ μm, cavity lengths $2a = 10$, 15, and 20 mm, and 100 μm thick bottom layer below the cavity when subjected to 30% stretching. For $2a \geq 15$ mm, the shear and normal stresses are smaller than 2 kPa, i.e., the subject will not physically perceive the presence of the device for stretching up to 30%.

Utilizing these optimized designs, **Figure 5** provides demonstrations with functional devices. Namely, Figure 5a presents a photograph of a mechano-acoustic sensor that contains an accelerometer on a strain-isolated substrate at 30% stretch. Details of the fabrication process can be found in the Experimental Section, and Figures S5 and S15 (Supporting Information). The sample was stretched (30%), placed on a vibration generator, and subjected to incremental changes in vibration frequency in a sequence of 1, 5, 10, 50, 100, and 500 Hz for ≈5 s at each frequency (video in Figure S16, Supporting Information). The voltage output of the accelerometer, corresponding to motion in the out-of-plane direction, was recorded during this process (Figure S17, Supporting Information). Standard software (AD Instruments LabChart 8, Colorado Springs, CO) was implemented to detect the location of peaks from the voltage measurements. The frequency of these peaks was then plotted as a function of time, as shown in Figure 5b. The performance of the mechano-acoustic sensor, as assessed by its
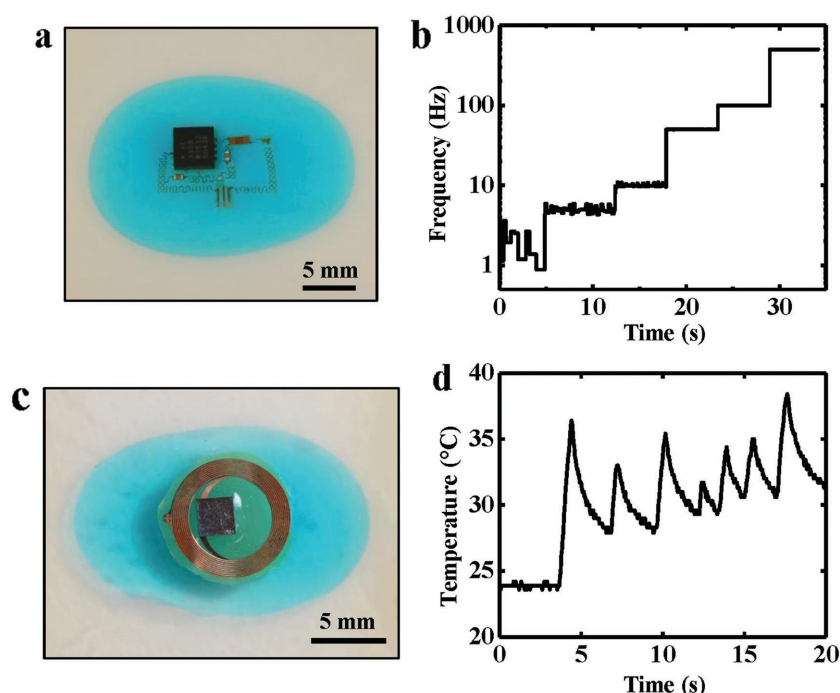
Figure 5. Device demonstrations. a) Photograph of a mechano-acoustic sensor at 30% stretch and b) corresponding measured frequencies while subjected to vibrations at different frequencies induced using a vibration generator. c) Photograph of a wireless temperature sensor at 40% stretch and d) corresponding measured temperatures while heated to various levels with a heat gun.

dramatically reduced interface stresses and associated improved wearability in skin-mounted devices. Ionic liquids offer exceptionally low vapor pressures and negligible permeability through commonly used elastomers, thereby ensuring robust, long-term operation without leakage or evaporation. Systematic theoretical and experimental studies of these cavities reveal a set of key design parameters for their integrity, without collapse. For given device and cavity dimensions, analytic modeling provides guidelines for optimizing the thickness of the cavity. The strain-isolation effects studied by FEA suggest 2/3 as an appropriate choice for the normalized length of the device (L/a) for the purpose of preventing the interfacial stresses on the skin from reaching thresholds for sensation (2 kPa), for typical levels of deformation. Device demonstrations of these ionic liquid-filled cavity concepts in wireless and wired sensing platforms has been applied to a NFC device mounted on a phantom skin.

ability to correctly measure the applied vibration frequency, was nearly identical for substrates without ionic liquid (no strain-isolation) at 0% stretch, with ionic liquid at 0% stretch, and with ionic liquid at 30% stretch (Figures S17–S20, Supporting Information). In all of these cases, the frequencies applied to the sample through the vibration generator could be accurately measured with the exception of low frequencies of 1 Hz and less, due to the sensitivity limit (0.5 to 550 Hz) of the accelerometer itself.

An additional demonstration involves the liquid-filled substrates integrated with an NFC device, as shown at 40% stretch in Figure 5c. The electronics incorporate an NFC bare die (SL13A, AMS AG, Cupertino, CA) with built-in temperature-measurement capabilities connected to a Cu coil that allows for wireless transfer of data. Details of the fabrication process can be found in the Experimental Section. Figure 5d shows temperature data collected wirelessly as the sample is subjected to incremental changes in temperature by repetitive heating with a heat gun, as shown in the video in Figure S21 (Supporting Information). The data collected in the stretched state (40%) are similar to those collected in the undeformed state (Figure S20, Supporting Information). Overall, these results illustrate the effectiveness of this strain-isolation strategy in practical applications, even under large deformation.

3. Conclusions

Liquid-filled cavities located within a soft, elastomeric enclosure and positioned between electronics above and skin below provide excellent levels of strain-isolation, for

4. Experimental Section

Preparation of Liquid-Filled Substrates: Figure S5 (Supporting Information) shows the technical approach for fabricating liquid-filled substrates for strain-isolation. First (Step 1 in Figure S5, Supporting Information), photolithography defined a pattern in an SU-8 mold, e.g., for a 100 μm thick feature: SU-8 2100 photoresist (MicroChem, Westborough, MA), spin-cast at 3000 rpm for 30 s, baked at 65 °C for 5 min and 95 °C for 20 min, UV exposed to 240 mJ cm^{-2}, postexposure baked at 65 °C for 5 min and 95 °C for 10 min, developed for ≈10 min in SU-8 developer, IPA rinsed, and hard-baked at 150 °C for 10 min. Spin-casting poly(methyl methacrylate) 495 A8 (MicroChem, Westborough, MA) at 3000 rpm for 30 s and baking at 110 °C for 5 min and 150 °C for 3 min formed a thin antiadhesive layer on the mold (Step 2). An additional spin-casting on top of the mold and curing at room temperature for 4 h yielded a silicone-based substrate (Ecoflex 00–30, Smooth-On, Macungie, Pennsylvania, mixed in a ratio of 1:1) of a desired thickness, as governed by the spin speed (Step 3). Delamination from the SU-8 mold allowed sample placement on a silicon wafer with the feature side facing up (Step 4). A physical barrier (e.g., Kapton film) masked the cavity regions while a thin layer of Ecoflex produced a bonding layer (Step 5). Subsequent removal of the physical mask left the cavity region with no "bonding" layer. Laminating a fully cured layer of Ecoflex onto the substrate and allowing the bonding layer of Ecoflex to cure resulted in a cavity in the substrate (Step 6). After fabrication of the desired device (see the following sections for more details), electron beam evaporation on the back-side of the device created a layer of 50 nm of SiO$_2$. Ultraviolet ozone (UVO) exposure of the Ecoflex substrate and the back-side of the device allowed for strong bonding of the device

to the strain-isolating substrate. As a result, we observed no evidence of delamination between our devices and the substrates during the experiments. A syringe injected ionic liquid (1-ethyl-3-methylimidazolium ethyl sulfate [EMIM][EtSO$_4$], Sigma-Aldrich, St. Louis, Missouri) into the cavity to a desired volume (Step 7). Upon removal of the syringe, the compliant substrate naturally sealed the hole (i.e., it elastically rebounded) such that ionic liquid did not leak. An additional amount of Ecoflex could be applied to enhance the sealing.

Fabrication and Testing of the NFC Device: A Cu (18 μm)/PI (12 μm)/Cu (18 μm) foil provided the starting material for the coils. Photolithography and wet etching formed inductive coil patterns in Cu on each side, and electroplating through a VIA hole joined the two sides to form a dual-layered coil. For more details on the fabrication process, please see ref. [44].[44] An oxide remover (Flux, Worthington, Columbus, OH) cleaned the contact openings for the thinned NFC bare dies. An In/Ag solder paste (Ind. 290, Indium Corporation, Chicago, IL) attached the dies (100 μm thick, SL13A, AMS AG, Cupertino, CA) to the device. A small amount of a silicone-based elastomer (Q1-4010, Dow Corning, Auburn, MI) served as an encapsulant for the dies and coils.

A heat gun subjected the samples to incremental changes in temperature. An NFC/HF reader (AS3911B, AMS AG, Cupertino, CA) connected to a laptop enabled wireless acquisition of temperature data during the experiment. See video (Figure S21) of the Supporting Information for a demonstration of the experiments.

Fabrication and Testing of the Mechano-Acoustic Sensor: Fabrication of mechano-acoustic sensors included patterning of the interconnects, transfer-printing of key components, and bonding of the component chips. Interconnect patterning began with a commercial laminate (Microthin, Oak Mitsui Inc., Hoosick Falls, New York) that contains a copper carrier film (17.5 μm) and a thin copper foil (3 μm) separated by an ultrathin release layer. Spin-coating and thermal curing formed a film of polyimide (1.2 μm, PI 2545, HD Microsystems, Parlin, NJ) on the side with the thin copper foil (3 μm). Peeling this PI-coated layer from the thick copper layer allowed its attachment onto a glass slide coated with poly(dimethylsiloxane) (Sylgard 184, Dow Corning, Auburn, MI). Photolithography and metal etching defined a pattern of interconnects in the copper. Another spin-coating and curing process yielded a uniform layer of PI on the resulting pattern. Photolithography and reactive ion etching (March, Nordson, Carlsbad, CA) produced top and bottom layers of PI that support and encapsulate the interconnects with the soldering pads exposed. In the transfer-printing step, water-soluble tape (Aquasol, North Tonawanda, NY) facilitated transfer of these encapsulated interconnects onto the strain-isolated substrates via UVO treatment as described in the Experimental Section "Preparation of Strain–Isolation Structures." Removal of the tape by immersion in water exposed the interconnects (Figure S15a, Supporting Information). A solder paste (Ind. 290, Indium Corporation, Chicago, IL) heated with a heat gun at ≈165 °C bonded the device components onto designated pads (Figure S15b, Supporting Information). Soldering also connected the copper wires to the device to enable testing (Figure S15e, Supporting Information).

Tests involved placing the devices on a flat, aluminum stand (4 cm × 4 cm) mounted on a vibration generator (3B Scientific, Tucker, Georgia). A 1 cm pole attached to the diaphragm of a loud speaker (SR 1010, Somogyi, 50 W, 100 mm, 8 Ω) and fitted inside a plastic housing generated the vibrations. The sine-wave output of a function generator (FG100, 3B Scientific, Tucker, Georgia) provided 3 V output to the loud speaker at discrete frequencies of 1, 5, 10, 50, 100, and 500 Hz. A commercial system (Powerlab, ADInstruments, Colorado Springs, CO) enabled data acquisition without filters at a sampling rate of 1 kHz.

[1] MC10, Inc., http://mc10inc.com (accessed: September 2016).
[2] BBC, L'Oreal unveils superthin smart skin patch, http://www.bbc.com/news/technology-35238636 (accessed: September 2016).
[3] NCC, Electronic skin makes your body a computer, http://www.cnn.com/2015/05/15/tech/electronic-skin/ (accessed: September 2016).
[4] A. Chortos, Z. Bao, *Mater. Today* **2014**, *17*, 321.
[5] C. Pang, J. H. Koo, A. Nguyen, J. M. Caves, M. G. Kim, A. Chortos, K. Kim, P. J. Wang, J. B. H. Tok, Z. Bao, *Adv. Mater.* **2015**, *27*, 634.
[6] W. Gao, S. Emaminejad, H. Y. Y. Nyein, S. Challa, K. V. Chen, A. Peck, H. M. Fahad, H. Ota, H. Shiraki, D. Kiriya, D. H. Lien, G. A. Brooks, R. W. Davis, A. Javey, *Nature* **2016**, *529*, 509.
[7] J. T. Muth, D. M. Vogt, R. L. Truby, Y. Menguc, D. B. Kolesky, R. J. Wood, J. A. Lewis, *Adv. Mater.* **2014**, *26*, 6307.
[8] R. C. Webb, Y. Ma, S. Krishnan, Y. Li, S. Yoon, X. Guo, X. Feng, Y. Shi, M. Seidel, N. H. Cho, J. Kurniawan, J. Ahad, N. Sheth, J. Kim, J. G. Taylor, T. Darlington, K. Chang, W. Huang, J. Ayers, A. Gruebele, R. M. Pielak, M. J. Slepian, Y. Huang, A. M. Gorbach, J. A. Rogers, *Sci. Adv.* **2015**, *1*, e1500701.
[9] A. Chortos, J. Liu, Z. Bao, *Nat. Mater.* **2016**, *15*, 937.
[10] Y. H. Chen, B. W. Lu, Y. Chen, X. Feng, *IEEE Electron Device Lett.* **2016**, *37*, 496.
[11] H. Y. Y. Nyein, W. Gao, Z. Shahpar, S. Emaminejad, S. Challa, K. Chen, H. M. Fahad, L. C. Tai, H. Ota, R. W. Davis, A. Javey, *ACS Nano* **2016**, *10*, 7216.
[12] C. H. Lee, Y. J. Ma, K. I. Jang, A. Banks, T. Pan, X. Feng, J. S. Kim, D. Kang, M. S. Raj, B. L. McGrane, B. Morey, X. Y. Wang, R. Ghaffari, Y. G. Huang, J. A. Rogers, *Adv. Funct. Mater.* **2015**, *25*, 3698.
[13] D. H. Kim, N. S. Lu, R. Ma, Y. S. Kim, R. H. Kim, S. D. Wang, J. Wu, S. M. Won, H. Tao, A. Islam, K. J. Yu, T. I. Kim, R. Chowdhury, M. Ying, L. Z. Xu, M. Li, H. J. Chung, H. Keum, M. McCormick, P. Liu, Y. W. Zhang, F. G. Omenetto, Y. G. Huang, T. Coleman, J. A. Rogers, *Science* **2011**, *333*, 838.
[14] C. Wang, D. Hwang, Z. B. Yu, K. Takei, J. Park, T. Chen, B. W. Ma, A. Javey, *Nat. Mater.* **2013**, *12*, 899.

[15] B. C. K. Tee, A. Chortos, A. Berndt, A. K. Nguyen, A. Tom, A. McGuire, Z. L. C. Lin, K. Tien, W. G. Bae, H. L. Wang, P. Mei, H. H. Chou, B. X. Cui, K. Deisseroth, T. N. Ng, Z. Bao, *Science* **2015**, *350*, 313.

[16] A. P. Gerratt, H. O. Michaud, S. P. Lacour, *Adv. Funct. Mater.* **2015**, *25*, 2287.

[17] A. Cyganowski, I. R. Minev, N. Vachicouras, K. Musick, S. P. Lacour, *11th IEEE Sensors Conf.*, IEEE, Taipei, Taiwan **2012**.

[18] S. S. Yao, Y. Zhu, *Adv. Mater.* **2015**, *27*, 1480.

[19] F. Xu, Y. Zhu, *Adv. Mater.* **2012**, *24*, 5117.

[20] C. Wu, L. J. Fang, X. Y. Huang, P. K. Jiang, *ACS. Appl. Mater. Interfaces* **2014**, *6*, 21026.

[21] T. Sekitani, Y. Noguchi, K. Hata, T. Fukushima, T. Aida, T. Someya, *Science* **2008**, *321*, 1468.

[22] T. Sekitani, H. Nakajima, H. Maeda, T. Fukushima, T. Aida, K. Hata, T. Someya, *Nat. Mater.* **2009**, *8*, 494.

[23] D. Y. Khang, H. Q. Jiang, Y. Huang, J. A. Rogers, *Science* **2006**, *311*, 208.

[24] M. Kaltenbrunner, T. Sekitani, J. Reeder, T. Yokota, K. Kuribara, T. Tokuhara, M. Drack, R. Schwodiauer, I. Graz, S. Bauer-Gogonea, S. Bauer, T. Someya, *Nature* **2013**, *499*, 458.

[25] L. Lin, S. Y. Liu, S. R. Fu, S. M. Zhang, H. Deng, Q. Fu, *Small* **2013**, *9*, 3620.

[26] H. C. Ko, M. P. Stoykovich, J. Z. Song, V. Malyarchuk, W. M. Choi, C. J. Yu, J. B. Geddes, J. L. Xiao, S. D. Wang, Y. G. Huang, J. A. Rogers, *Nature* **2008**, *454*, 748.

[27] R. Li, M. Li, Y. W. Su, J. Z. Song, X. Q. Ni, *Soft Matter* **2013**, *9*, 8476.

[28] Y. H. Zhang, S. D. Wang, X. T. Li, J. A. Fan, S. Xu, Y. M. Song, K. J. Choi, W. H. Yeo, W. Lee, S. N. Nazaar, B. W. Lu, L. Yin, K. C. Hwang, J. A. Rogers, Y. G. Huang, *Adv. Funct. Mater.* **2014**, *24*, 2028.

[29] Y. Chen, B. W. Lu, Y. H. Chen, X. Feng, *Sci. Rep.* **2015**, *5*, 594601.

[30] Y. Liu, Z. Yan, Q. Lin, X. Guo, M. Han, K. Nan, K. C. Hwang, Y. Huang, Y. H. Zhang, J. A. Rogers, *Adv. Funct. Mater.* **2016**, *26*, 2909.

[31] B. Y. Ahn, E. B. Duoss, M. J. Motala, X. Y. Guo, S. I. Park, Y. J. Xiong, J. Yoon, R. G. Nuzzo, J. A. Rogers, J. A. Lewis, *Science* **2009**, *323*, 1590.

[32] A. Robinson, A. Aziz, Q. Liu, Z. Suo, S. P. Lacour, *J. Appl. Phys.* **2014**, *115*, 143511.

[33] A. Romeo, Q. H. Liu, Z. G. Suo, S. P. Lacour, *Appl. Phys. Lett.* **2013**, *102*, 131904.

[34] S. Xu, Y. H. Zhang, L. Jia, K. E. Mathewson, K. I. Jang, J. Kim, H. R. Fu, X. Huang, P. Chava, R. H. Wang, S. Bhole, L. Z. Wang, Y. J. Na, Y. Guan, M. Flavin, Z. S. Han, Y. G. Huang, J. A. Rogers, *Science* **2014**, *344*, 70.

[35] Sigma-Aldrich Co. LLC., http://www.sigmaaldrich.com/content/dam/sigma-aldrich/docs/Aldrich/Brochure/al_chemfile_v6_n9.pdf (accessed: September 2016).

[36] O. Cabeza, E. Rilo, J. Vila, L. Segade, E. López-Lago, L. M. Varela, M. Vilas, E. Tojo, *The 18th Int. Electronic Conf. on Synthetic Organic Chemistry*, MDPI, Santiago de Compostela, Spain **2014**.

[37] ABAQUS Analysis User's Manual, V6.10, **2010**.

[38] E. S. Dellon, R. Mourey, A. L. Dellon, *Plast. Reconstr. Surg.* **1992**, *90*, 112.

[39] K. Atsushi, A. Noriyoshi, K. Tadashi, *J. Hand Therapy* **2005**, *18*, 421.

[40] Y. G. Y. Huang, W. X. Zhou, K. J. Hsia, E. Menard, J. U. Park, J. A. Rogers, A. G. Alleyne, *Langmuir* **2005**, *21*, 8058.

[41] Q. M. Wang, X. H. Zhao, *Phys. Rev. E* **2013**, *88*, 042403.

[42] J. Restolho, J. L. Mata, B. Saramago, *J. Colloid Interface Sci.* **2009**, *340*, 82.

[43] S. D. Wang, M. Li, J. Wu, D. H. Kim, N. S. Lu, Y. W. Su, Z. Kang, Y. G. Huang, J. A. Rogers, *J. Appl. Mech.-T. ASME* **2012**, *79*, 031022.

[44] J. Kim, A. Banks, H. Y. Cheng, Z. Q. Xie, S. Xu, K. I. Jang, J. W. Lee, Z. J. Liu, P. Gutruf, X. Huang, P. H. Wei, F. Liu, K. Li, M. Dalal, R. Ghaffari, X. Feng, Y. G. Huang, S. Gupta, U. Paik, J. A. Rogers, *Small* **2015**, *11*, 906.